JACS Au
AN OPEN ACCESS JOURNAL OF THE AMERICAN CHEMICAL SOCIETY

Editors' Choice
Open Access

pubs.acs.org/jacsau
Article

Inverse Design of 2D Altermagnetic Metal−Organic Framework Monolayers from Hückel Theory of Nonbonding Molecular Orbitals

Yixuan Che, Yilin Chen, Xin Liu, Haifeng Lv,* Xiaojun Wu,* and Jinlong Yang

Cite This: JACS Au 2025, 5, 381−387
Read Online

ACCESS | Metrics & More | Article Recommendations | Supporting Information

ABSTRACT: Altermagnets, characterized by spontaneous spin-splitting without net magnetization, are challenging to realize due to their unique spin group symmetries. Two-dimensional (2D) magnetic metal−organic frameworks (MOFs), with tunable topologies and spins, offer promising platforms for achieving altermagnetism. In this study, we propose a general strategy to create 2D altermagnetic monolayers by bridging Cr with organic ligands exhibiting nonbonding molecular orbitals (NBMOs) based on the Hückel molecular orbital theory and first-principles calculations. Three 2D MOFs, namely, $Cr(diz)_2$, $Cr(c\text{-}pyr)_2$, and $Cr(f\text{-}pid)_2$ (diz = 1,3-diazete, *c*-pyr = pyrrolo[3,4-*c*]pyrrole, *f*-pid = pyrrolo[3,4-*f*]isoindole), are constructed using this strategy and exhibit the altermagntic ground state. These MOFs possess the spin point group ${}^{2}\bar{4}{}^{1}m{}^{2}2$ and exhibit critical temperatures reaching up to 183 K. Analyses of orbital symmetry and energy levels rationalize the presence of altermagnetism. Our findings highlight the critical role of NBMOs in realizing 2D-MOF-based altermagnets with enhanced critical temperatures.

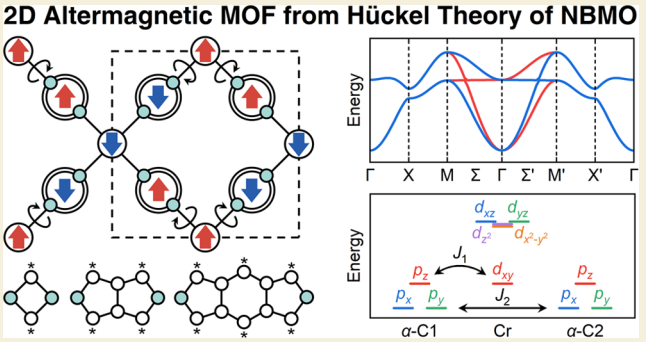

KEYWORDS: *altermagnetism, two-dimensional materials, metal−organic frameworks, nonbonding molecular orbitals, first-principles calculation*

INTRODUCTION

Altermagnets, a recently proposed class of magnetic materials characterized by spontaneous spin-splitting without net magnetization, hold great promise for spintronic applications due to their unique spin group symmetry.[1−6] In altermagnets, sublattices opposite (α and β) spins are connected by rotational symmetry, while inversion and pure translation symmetries are prohibited. This restricts altermagnets to 37 unique spin point groups, where the sublattice point group is always a subgroup of the crystalline group with an index of 2.[1] For example, an altermagnet can be obtained if the sublattice with the point group *mmm* can rotate around a 4-fold axis, leading to a ${}^{2}4/{}^{1}m{}^{1}m{}^{2}m$ spin point group.[7] Despite the well-defined symmetry requirements, recent reports on altermagnets have mainly focused on individual materials or high-throughput screening approaches.[5−12] Achieving a collection of systems that meet these magnetic symmetries remains a significant challenge.

Metal−organic frameworks (MOFs), assembled from various ligands and metal nodes, offer tunable magnetism and topology.[13−18] In two-dimensional (2D) motifs, a total of 36 tessellations have been identified.[17] By judicious selection of chemical components, 2D MOFs with diverse magnetic orders, including ferromagnetism,[19−21] ferrimagnetism,[22−25] altermagnetism,[26] and antiferromagnetism,[21,27] can be realized. These properties make 2D MOFs ideal platforms for obtaining magnets with unique characteristics, such as spin liquidity,[28] canted antiferromagnetism,[29] and topological magnetism.[25,30] However, the inverse design of 2D MOFs with desired magnetism at the molecular level remains challenging.

Orbital interactions are crucial in modulating magnetic interactions in 2D magnetic MOFs due to their coordination mode, including $d-p$ in ferrimagnetism,[22,24,25] $d-\pi$ in ferromagnetism,[31] and $d-d$ 180° superexchange in antiferromagnetism.[27] While delocalized orbitals extending through entire ligand molecules contribute to strong $d-p$ and $d-p-d$ exchange in 2D MOFs, $p-p$ exchange is relatively weak.[22,26,27] Manipulating $p-p$ interaction using the localized molecular orbital of ligands provides an alternative magnetic pathway to achieve targeted magnetic order in 2D MOFs.

Nonbonding molecular orbitals (NBMOs) play an essential role in defining electron localization, according to Hückel molecular orbital (HMO) theory.[32,33] By solving a linear

Received: November 27, 2024
Accepted: December 30, 2024
Published: January 15, 2025

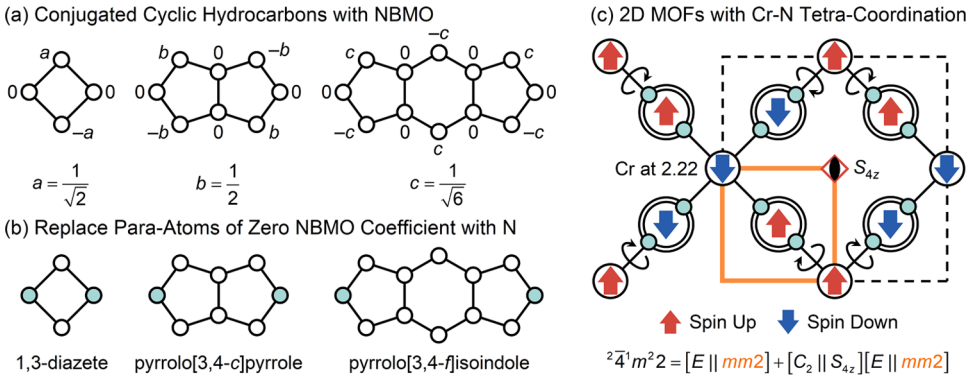

Figure 1. Workflow of designing altermagnetic 2D MOFs. (a) Frameworks of conjugated hydrocarbons with NBMOs. (b) Para-atoms with zero NBMO coefficient (green dots) are equivalently replaced with N to tetracoordinate with Cr. (c) Schematic structure of the resulting 2D MOFs.

system of equations, NBMO coefficients can be calculated to clarify the orbital contribution of each atom, where larger absolute coefficients signify greater contributions.[34] In this study, we present three 2D Cr-based MOF monolayers exhibiting altermagnetic ground state, designed using organic ligands with NBMOs and first-principles calculations (Note S1 in the Supporting Information). Initially, three molecules are considered, including 1,3-cyclobutadiene, pentalene, and *s*-indacene. By substituting para-atoms (with zero NBMO coefficients) with nitrogen and coordinating them tetrahedrally with Cr, three 2D MOFs are obtained, including Cr(diz)$_2$, Cr(*c*-pyr)$_2$, and Cr(*f*-pid)$_2$ (diz = 1,3-diazete, *c*-pyr = pyrrolo[3,4-*c*]pyrrole, and *f*-pid = pyrrolo[3,4-*f*]isoindole). The magnetic moment on the organic ligands is mostly contributed by α-carbon atoms (α-C, the nearest neighbor of nitrogen), and an antiparallel spin alignment between the organic rings is observed. The altermagnetic ground state and spin-splitting are protected by the spin point group of $^{2}\bar{4}^{1}m^{2}2$. Additionally, *d*−*p* interactions between central Cr and linkers enhance the critical temperatures of the MOFs. Using Monte Carlo simulations within the Heisenberg model, the critical temperatures of three MOFs are estimated to be 183, 177, and 112 K, respectively. Further analyses of the orbital energy levels and symmetry explain the magnetic exchange interactions.

RESULTS AND DISCUSSION

Design Strategy and Structures

As illustrated in Figure 1, the MOF monolayers are constructed from conjugated hydrocarbons with D_{2h} symmetry, including 1,3-cyclobutadiene, pentalene, and *s*-indacene. Based on the HMO theory with NBMOs, the NBMO coefficients can be derived (Figure 1a and Note S2 in the Supporting Information).[34] For 1,3-cyclobutadiene, there is a pair of NBMO with a coefficient of $1/\sqrt{2}$. Pentalene has three rings and one NBMO with a coefficient of 1/2. *S*-indacene, a derivative structure of pentalene with an additional six-membered ring, also has one NBMO with a coefficient of $1/\sqrt{6}$. All three molecules contain para-atoms with a zero NBMO coefficient and α-C atoms with a nonzero coefficient.

To form coordination bonds between metal and organic linkers, para-carbon atoms (with zero NBMO coefficients) are equivalently replaced with nitrogen atoms, resulting in 1,3-diazete (diz), pyrrolo[3,4-*c*]pyrrole (*c*-pyr), and pyrrolo[3,4-*f*]isoindole (*f*-pid, Figure 1b). Planar tetracoordination between Cr and organic ligands is investigated with a 2D square motif, leading to the formation of Cr(diz)$_2$, Cr(*c*-pyr)$_2$, and Cr(*f*-pid)$_2$, respectively (Figure S1 and Tables S1−S3). As shown in Figure 1c, organic ligands can rotate around the Cr atoms. Table 1 summarizes the calculated structural parameters of the three MOFs, including lattice parameters, bond lengths between Cr and N atoms, sheet thicknesses, and torsion angles. The lattice parameter and torsion angle increase with the size of the organic linker.

Table 1. Calculated Parameters of Three Altermagnetic 2D MOFs, Including Lattice Parameters (a for Length and α for Angle, in Å and °, Respectively), Bond Lengths between Cr and N atoms (L_1 and L_2, in Å), Sheet Thicknesses (d, in Å), Torsion Angles (θ, in °), Bader Charge Transfer from the Cr to Organic Ligands (C, in e$^-$), Formation Energies ($\mathcal{E}_{form}$, in eV per Stoichiometric Formula), and Electronic Band Gaps ($\mathcal{E}_g$, in eV)[a]

	Cr(diz)$_2$	Cr(*c*-pyr)$_2$	Cr(*f*-pid)$_2$
a	8.69	11.93	15.33
α	90.00	90.00	90.00
L_1	2.0328	2.0597	2.0625
L_2	2.0378	2.0673	2.0646
d	2.26	2.74	3.48
θ	34.07	40.55	42.96
C	1.374	1.225	1.368
$\mathcal{E}_{form}$	−10.65	−7.65	−7.07
$\mathcal{E}_g$	2.85	1.88	1.40

[a]Structural parameters are labeled in Figure S1. The values of $\mathcal{E}_g$ are calculated with the HSE06 hybrid functional.

Stabilities

To examine the stabilities of 2D MOFs, the average formation energy per stoichiometric formula ($\mathcal{E}_{form}$) is calculated as

$$\mathcal{E}_{form} = \frac{\mathcal{E}_{MOF} - (2\mathcal{E}_{Cr} + 4\mathcal{E}_{mole})}{2} \quad (1)$$

where $\mathcal{E}_{MOF}$, $\mathcal{E}_{Cr}$, and $\mathcal{E}_{mole}$ denote the energies of 2D MOFs, Cr atoms, and organic molecules, respectively. This formula corresponds to the chemical equation Cr + 2 × molecule → Cr(molecule)$_2$. The calculated formation energies, ranging from −7.07 to −10.65 eV (Table 1), are higher than that of Cr(pyz)$_2$, indicating the feasible formation of the three MOFs from Cr and ligands.[24] Figure S2 presents the temperature, reaction time, solvent, and additive conditions predicted by the

https://doi.org/10.1021/jacsau.4c01150
JACS Au 2025, 5, 381−387

MOF synthesis prediction tool.[35] Moreover, to assess experimental feasibility, we modeled a self-assembled heterostructure of $Cr(c\text{-pyr})_2$ on an Ag(100) surface manually constructed based on two recent related works,[36,37] in which the exfoliation energy is calculated as 37.47 meV $Å^{-2}$, comparable to that of black phosphorus (Figure S3).[38] This suggests that the proposed MOFs could potentially be synthesized and exfoliated from the substrates.

Structural dynamic stability is confirmed via phonon spectrum analysis, showing no obvious imaginary frequencies (Figure S4). Thermal stability is demonstrated using *ab initio* molecular dynamic (AIMD) simulations, with the 2D MOFs maintaining structural integrity up to 600 K for $Cr(diz)_2$ and $Cr(c\text{-pyr})_2$ (Figures S5 and S6), and up to 900 K for $Cr(f\text{-pid})_2$ (Figure S7). Additionally, the relaxed structures are most stable at a specific torsion angle, with $Cr(f\text{-pid})_2$ exhibiting the smallest energy difference at 90°, indicating its highest AIMD temperature (Figure S8). Notably, the sudden decrease in energy for $Cr(diz)_2$ at approximately 2 ps indicates bonding between adjacent ligands.

Mechanical stability is assessed by using the stress−strain method to calculate elastic constants C_{11}, C_{12}, and C_{66}. For $Cr(diz)_2$, these values are 40.33, 37.92, and 35.91 N m^{-1}, respectively. For $Cr(c\text{-pyr})_2$, they are 35.20, 34.03, and 31.76 N m^{-1}. For $Cr(f\text{-pid})_2$, the values are 30.68, 30.65, and 28.59 N m^{-1}. All values satisfy the elastic stability conditions of a tetragonal 2D crystal ($C_{11} > 0$, $C_{66} > 0$, $C_{11} > |C_{12}|$), confirming mechanical stability.[39]

Magnetic Properties

To determine the magnetic ground state, eight magnetic orders are considered, including one ferromagnetic phase, one antiferromagnetic phase, four ferrimagnetic phases, one altermagnetic phase, and one nonmagnetic phase (Figure S9). These magnetic states are categorized into four types based on the magnetic configuration of the organic ligands. Type I features a full parallel arrangement between the neighboring rings. Type II exhibits no magnetism. Type III and IV consist of two spin-up and spin-down rings with different arrangements, resulting in tetragonal and orthorhombic phases, respectively.

Table 2 summarizes the relative energy differences of these orders, indicating the altermagnetic state is the ground state in all three MOFs. The antiparallel magnetic moments of Cr atoms lead to a real space point group of $\bar{4}m2$ and a sublattice point group of $mm2$. Thus, the spin point group is

$$^{2}\bar{4}^{1}m^{2}2 = [E\|mm2] + [C_2\|S_{4z}][E\|mm2] \quad (2)$$

where the superscript denotes the symmetry of the magnetic state.[1,40] This symmetry is reflected in the spin-splitting of the band structures (Figure 2). The valence band maximum (VBM) splits into opposite polarizations but with the same magnitude along only the Γ−(Σ)−M and Γ−(Σ′)−M′ path directions, i.e., paths corresponding to the spin-up/down channel arrangement, due to the tetragonal spin point group. The spin-splitting magnitudes of the VBM band for $Cr(diz)_2$, $Cr(c\text{-pyr})_2$, and $Cr(f\text{-pid})_2$ are 16.48, 30.86, and 37.54 meV, respectively, comparable to those of altermagnetic semiconductors La_2CuO_4 (10 meV),[1] $LaMnO_3$ (20 meV),[41,42] and κ-Cl (50 meV).[8]

Table 2. Magnetic Energies (in meV per Unit Cell) of Eight Different Magnetic States Relative to the Altermagnetic Ground State, along with the Deduced Magnetic Exchange Parameters (J, in meV) and Magnetic Anisotropy Parameter (D, in μeV)[a]

	$Cr(diz)_2$	$Cr(c\text{-pyr})_2$	$Cr(f\text{-pid})_2$
AM	0	0	0
FM	152.44	168.67	81.28
FiM (I)	274.35	233.32	165.78
FiM (II)	125.96	175.86	110.98
NM	7601.55	7955.11	8153.67
FiM (III)	88.12	26.36	13.80
FiM (IV)	147.41	111.87	70.31
AFM	60.22	86.59	57.22
J_1	−7.6914	−4.0407	−5.2813
J_2	62.6375	87.3175	54.8650
J_3	2.7538	0.8238	0.4313
J_4	2.4176	0.7276	−2.3550
D	75.88	75.28	75.52

[a]AM: altermagnetic; FM: ferromagnetic; FiM: ferrimagnetic; AFM: antiferromagntic; NM: nonmagnetic.

Electronic Structure and Magnetic Moments

$Cr(diz)_2$, $Cr(c\text{-pyr})_2$, and $Cr(f\text{-pid})_2$ are semiconductors with band gaps ($\mathcal{E}_g$) of 2.85, 1.88, and 1.40 eV, respectively. The density of states (DOS) in Figure S10 shows that in $Cr(c\text{-pyr})_2$ and $Cr(f\text{-pid})_2$, the DOS near the Fermi level ($\mathcal{E}_F$) is mainly contributed by carbon atoms. For $Cr(diz)_2$, the DOS at the conduction band minimum (CBM) is mainly from carbon, while at VBM, it is mainly from Cr and C. As the ligand size increases, the energy level of Cr near the VBM deepens, and the energy level gap between Cr and C widens. The band gap value also decreases from $Cr(diz)_2$ to $Cr(f\text{-pid})_2$.

Spin density and atomic magnetic moments (Figure S11a−c and Table S4) indicate that Cr transfers about two electrons to ligands, resulting in a magnetic moment of approximately 3.6 μ_B. The magnetic moment on the ligands mainly originates from the α-C atoms. For $Cr(f\text{-pid})_2$, γ-C atoms contribute the second largest magnetization. This corresponds to the nonzero NBMO coefficients, and the distribution of NBMO coefficients aligns closely with the charge density of the lowest unoccupied molecular orbital (LUMO) of each ligand molecule (Figure S11d−f). As the ligand size increases, the magnetic moment on Cr increases, while that on the organic ligands decreases.

The magnetic anisotropy energy (MAE) values indicate out-of-plane easy axes of $Cr(diz)_2$, $Cr(c\text{-pyr})_2$, and $Cr(f\text{-pid})_2$, with corresponding MAE values of 607.02, 602.27, and 604.19 μeV per unit cell, respectively (Table S5). These values are higher than those of $Cr(pyz)_2$ (482 μeV)[24] and $Cr(tdz)_2$ (494.1 μeV).[25] Note that there are also tiny magnetic anisotropies in the (001) plane at the level of about 10^{-8} eV.

Magnetic Transition Temperatures and Exchange Interactions

The magnetic transition temperatures are determined by a Monte Carlo simulation using the Heisenberg model. Due to the tetragonal symmetry, the spin Hamiltonian ($\mathcal{H}$) is expressed as

$$\mathcal{H} = \sum_k \sum_{\langle i,j \rangle} J_k S_i S_j + D_i S_{iz}^2 \quad (3)$$

https://doi.org/10.1021/jacsau.4c01150
JACS Au 2025, 5, 381−387

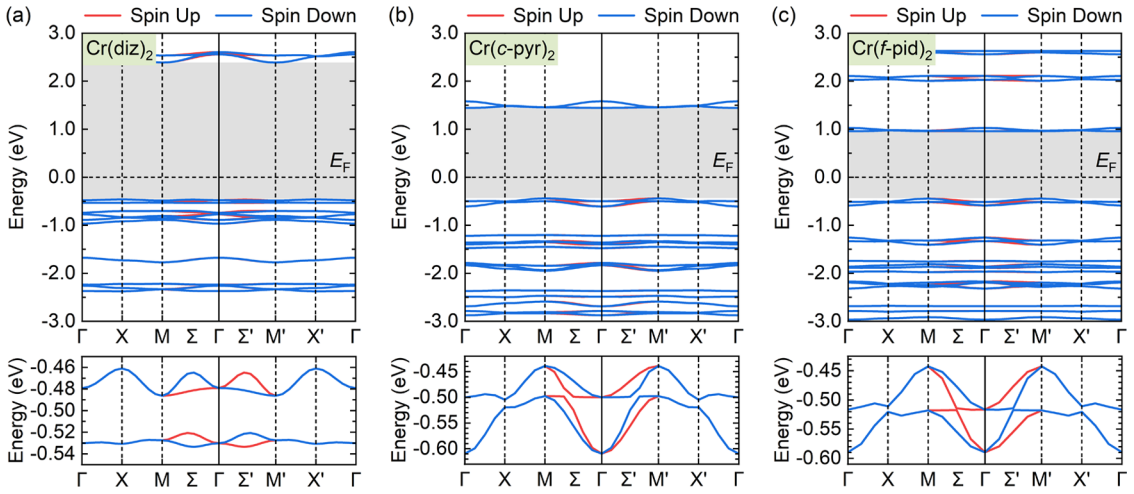

Figure 2. Band structures of 2D MOFs with the HSE06 functional. (a) $Cr(diz)_2$. (b) $Cr(c\text{-}pyr)_2$. (c) $Cr(f\text{-}pid)_2$. The gray shadows represent $\mathcal{E}_g$, and $\mathcal{E}_F$ is set to 0 eV.

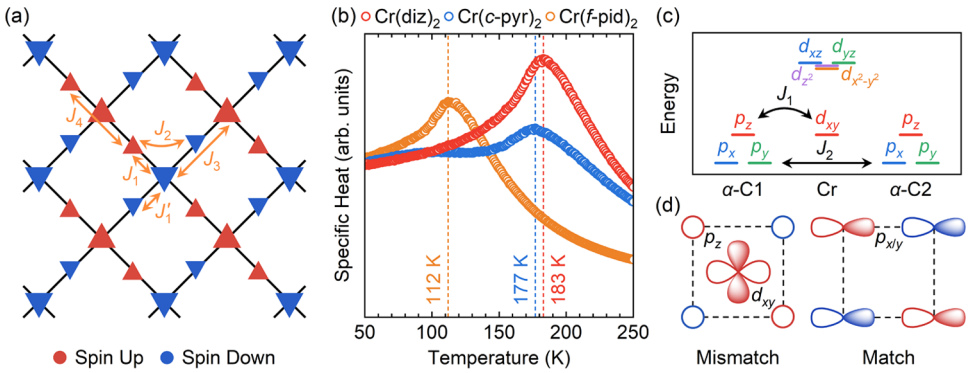

Figure 3. Magnetic exchange and transition temperatures. (a) Nearest and next-nearest neighbor spin exchanges (J_1 to J_4). (b) Specific heat versus temperature from Monte Carlo simulations. (c) Schematic of orbital energy level matching. (d) Orbital symmetry matching of d_{xy}–p_z (left panel) and p_x–p_x (or p_y–p_y) orbitals (right panel).

where J and S represent the exchange parameter and unit spin vectors along the c-axis, respectively. The S values for Cr and linkers are 2 and 1/2, respectively. D denotes the magnetic anisotropy parameter. Since the MAE from the organic ligands is relatively weak, only the MAE of Cr is considered in calculating D (with $S = 2$), and the MAE of ligands is assumed to be zero.

Four exchange parameters (J_1 to J_4) values are considered (Figure 3a and Note S1 in the Supporting Information). Although L_1 is not exactly equal to L_2, the difference between J_1 and J_1' is relatively small ($|J_1 - J_1'| < 1/10\ |J_1|$), so J_1' is treated equal to J_1 for simplicity. The calculated J and D are listed in Table 2, where J_2, the magnetic exchange between neighboring ligands, dominates. The D values of the three 2D MOFs are very similar. The specific heat curves in Figure 3b show that the magnetic transition temperatures for $Cr(diz)_2$, $Cr(c\text{-}pyr)_2$, and $Cr(f\text{-}pid)_2$ are 183, 177, and 112 K, respectively, much higher than those of 2D chromium trihalides (17 to 46 K).[43]

Orbital-resolved DOS of Cr and its α-C atoms are shown in Figure S12. To determine the energy level of different orbitals, band centers (ϵ) are calculated as

$$\epsilon = \frac{\int_{-\infty}^{\mathcal{E}_F} \mathcal{E} \times g(\mathcal{E}) d\mathcal{E}}{\int_{-\infty}^{\mathcal{E}_F} g(\mathcal{E}) d\mathcal{E}} \quad (4)$$

where $g(\mathcal{E})$ represents DOS and the energy window is set from $-\infty$ to $\mathcal{E}_F$. It is shown that the energy levels of Cr's d_{xy} and α-C's p_z orbitals, as well as α-C's p_x and p_y orbitals, are closely matched (Figure 3c). The former d_{xy}–p_z interaction corresponds to J_1, and the latter p–p interaction corresponds to J_2. Orbital symmetry matching in Figure 3d shows that the symmetry of the d_{xy}–p_z interaction does not match, while the p_x–p_x and p_y–p_y interactions do. Consequently, J_2 is larger than J_1, and the magnetic interaction between adjacent organic ligands dominates, resulting in a ground state of altermagnetism. Conversely, the strong d–p interaction in $Cr(pyz)_2$ and $Cr(tdz)_2$ makes their J_1 larger than J_2, leading to a ferrimagnetic ground phase.[24,25]

Interlayer Interactions

Beyond the intralayer interactions in monolayers, interlayer interactions in multilayer cases provide a more comprehensive understanding of magnetic exchange in 2D MOFs. Based on the experimentally synthesized $Cr(pyz)_2$,[23] an A-type multilayered $Cr(diz)_2$ is considered as an example, including interlayer ferromagnetic and antiferromagnetic order (Figure S13a). When the interlayer distance (d', defined as the distance

https://doi.org/10.1021/jacsau.4c01150
JACS Au 2025, 5, 381−387

between two Cr atoms along the stacking direction) is set to 7 Å, which is similar to that of experimental $Cr(pyz)_2$, the ferromagnetic order is more stable, with an energy difference of only 0.45 meV per unit cell, indicating a weak interlayer interaction (Figure S13b). The monolayer structure can be maintained within the calculation criteria.

When d' is manually set to 4 Å, closer to the case of $K_3Fe_2[PcFe\text{-}O_8]$[31] and much smaller than that of $Cr(pyz)_2$, $Cr(diz)_2$ prefers interlayer antiferromagnetism with an energy difference of 189.62 meV per unit cell (Figure S13c). However, since $Cr(diz)_2$ is not perfectly flat like layered $K_3Fe_2[PcFe\text{-}O_8]$, the forces between adjacent layers are too large (maximum of 0.125 eV $Å^{-1}$), causing multilayered structure distortion and forming interlayer C−C bonds with a distance of 1.67 Å (Figure S13d). Additionally, the interlayer antiferromagnetism will also lead to inversion between opposite spin sublattices ($[C_2||i]$), so it does not result in altermagnetism. This is reflected in the spin nondegeneracy and degeneracy of band structures (Figure S13e,f). Therefore, only the monolayer and intralayer interactions of Cr-MOFs are focused.

Extended Case Studies

To further verify the universality of designing MOF monolayers using NBMO, some extended cases are investigated involving different ligands and metals (Figures S14−S16 and Table S5). We first consider three extended molecules that meet the conditions of the HMO theory with NBMOs and construct three corresponding MOF monolayers. For cyclobuta[1,2-*c*:3,4-*c*′]dipyrrole (cdp) (Figure S14a), the NBMO coefficients of para-sites are nonzero ($1/\sqrt{6}$). $Cr(dpd)_2$ exhibits a ferrimagnetic ground state, with the magnetic moments on organic ligands mainly distributed on N and β-C atoms (Figure S14b,c).

For isoindolo[5,6-*f*]isoindole (iid), which adds an extra six-membered ring based of *f*-pid, the NBMO coefficients are similar to the previous cases, with para-sites having zero NBMO coefficients and minimal electron distribution (Figure S15a). The $Cr(iid)_2$ monolayer shows an altermagnetic ground state with the relative lowest energy among eight magnetic states, and the magnetic moment on ligands locates on α- and γ-C atoms (Figure S15b,c).

Additionally, a derivative molecule of iid, namely, pentaleno-[2,1-*c*:5,6,*c*′]dipyridine (pdp), also satisfies the HMO theory with NBMO, although it has a lower molecule point group of C_{2v}. Unlike iid with 5/6/6/5 fused rings, pdp has a 6/5/5/6 structure, leading to a different distribution of NBMO coefficients (Figure S16a). By equivalently replacing para-atoms with zero NBMO coefficient with nitrogen and connecting them with Cr nodes, the MOF monolayer $Cr(pdp)_2$ is also confirmed to be altermagnetism with the spin point group $^2m^2m^12$ (Figure S16b). Notably, the maximum magnetic moment of the organic ligand in $Cr(pdp)_2$ is located on the five-membered ring, where the NBMO coefficient is the largest ($2 \times 1/\sqrt{14}$, Figure S16c).

Moreover, to demonstrate the applicability of our design strategy to other transition metals, we tested a series of $M(c\text{-}pyr)_2$ monolayers with M = V, Cr, Mn, Fe, and Co (Table S6). The results indicate that our design strategy can achieve an altermagnetic ground state with other 3*d* metals. These extended case studies further illustrate the electron distribution retainability of molecules with NBMO in MOF monolayers and the universality of designing target magnetic ground states through such molecules.

Mechanical Properties

Further investigation reveals mechanical anisotropy in Young's modulus and Poisson's ratio (Figures S17−S19). The Young's modulus values of $Cr(diz)_2$, $Cr(c\text{-}pyr)_2$, and $Cr(f\text{-}pid)_2$ are 74.89, 66.25, and 59.18 N m^{-1}, respectively, equivalent to 331.37, 241.79, and 208.38 GPa by using sheet thickness, respectively. These values are comparable to that of the MoS_2 sheet (270 ± 100 GPa).[44] All three MOFs exhibit a minimal Poisson's ratio near zero, suggesting their excellent resistance to fracture and high resilience.

CONCLUSIONS

In summary, we propose a universal strategy for designing 2D altermagnetic MOF monolayers using organic molecules with nonbonding molecular orbitals. By constructing $Cr(diz)_2$, $Cr(c\text{-}pyr)_2$, and $Cr(f\text{-}pid)_2$, we demonstrate that the magnetic moments on the organic ligands are mainly located on α-C atoms, leading to the altered ground state. Due to the strong $p-p$ interaction between adjacent ligands and the presence of $d-p$ interaction, the magnetic transition temperature can reach up to 183 K. Further analyses of energy level and orbital symmetry matching rationalize the existence of altermagnetism through the competition between J_1 and J_2, elucidating the preference for altermagnetic ground state over ferrimagnetism. Our work not only presents a universal strategy for designing altermagnetic MOF monolayers with enhanced critical transition temperatures but also reveals the competitive nature of magnetic exchange interactions in determining the magnetic ground state.

ASSOCIATED CONTENT

Supporting Information

The Supporting Information is available free of charge at https://pubs.acs.org/doi/10.1021/jacsau.4c01150.

Computational methods; HMO theory with NBMOs; structural details; machine learning synthesis prediction; phonon band structures; AIMD simulations; energies with different torsion angles; magnetic configurations and moments; energies of different magnetic states; DOS and energy levels; spin density; multilayer cases with interlayer interaction; extended case studies; and mechanical and magnetic anisotropies (PDF)

AUTHOR INFORMATION

Corresponding Authors

Haifeng Lv − *School of Chemistry and Materials Science and State Key Laboratory of Precision and Intelligent Chemistry, CAS Key Laboratory of Materials for Energy Conversion, and Collaborative Innovation Center of Chemistry for Energy Materials (iChEM), University of Science and Technology of China, Hefei, Anhui 230026, China;* orcid.org/0000-0001-9491-6367; Email: hflv@ustc.edu.cn

Xiaojun Wu − *School of Chemistry and Materials Science and State Key Laboratory of Precision and Intelligent Chemistry, CAS Key Laboratory of Materials for Energy Conversion, and Collaborative Innovation Center of Chemistry for Energy Materials (iChEM), University of Science and Technology of China, Hefei, Anhui 230026, China; Hefei National Laboratory, University of Science and Technology of China, Hefei, Anhui 230088, China;* orcid.org/0000-0003-3606-1211; Email: xjwu@ustc.edu.cn

https://doi.org/10.1021/jacsau.4c01150
JACS Au 2025, 5, 381−387

Authors

Yixuan Che − *Hefei National Research Center for Physical Sciences at the Microscale, University of Science and Technology of China, Hefei, Anhui 230026, China;* orcid.org/0000-0002-3990-6868

Yilin Chen − *School of Chemistry and Materials Science, University of Science and Technology of China, Hefei, Anhui 230026, China;* orcid.org/0009-0001-3827-5152

Xin Liu − *School of Chemistry and Materials Science, University of Science and Technology of China, Hefei, Anhui 230026, China*

Jinlong Yang − *Hefei National Research Center for Physical Sciences at the Microscale, University of Science and Technology of China, Hefei, Anhui 230026, China; School of Chemistry and Materials Science and State Key Laboratory of Precision and Intelligent Chemistry, CAS Key Laboratory of Materials for Energy Conversion, and Collaborative Innovation Center of Chemistry for Energy Materials (iChEM), University of Science and Technology of China, Hefei, Anhui 230026, China; Hefei National Laboratory, University of Science and Technology of China, Hefei, Anhui 230088, China;* orcid.org/0000-0002-5651-5340

Complete contact information is available at: https://pubs.acs.org/10.1021/jacsau.4c01150

Author Contributions

Y.C., Y.C., and X.L. carried out the calculations and visualizations. H.L. and X.W. conceived the idea and supervised the work. All authors discussed the results and contributed to the manuscript.

Notes

The authors declare no competing financial interest.

■ ACKNOWLEDGMENTS

The research was supported by the National Natural Science Foundation of China (Grants No. 22225301 and 22303092), the Strategic Priority Research Program of the Chinese Academy of Sciences (Grant No. XDB0450101), the National College Student Innovation and Entrepreneurship Training Program (Grant No. 202310358043), the Innovation Program for Quantum Science and Technology (Grant No. 2021ZD0303302), the Fundamental Research Funds for the Central Universities, and Super Computer Center of USTCSCC and SCCAS.

■ REFERENCES

(1) Šmejkal, L.; Sinova, J.; Jungwirth, T. Beyond Conventional Ferromagnetism and Antiferromagnetism: A Phase with Nonrelativistic Spin and Crystal Rotation Symmetry. *Phys. Rev. X* **2022**, *12*, No. 031042.

(2) Šmejkal, L.; Sinova, J.; Jungwirth, T. Emerging Research Landscape of Altermagnetism. *Phys. Rev. X* **2022**, *12*, No. 040501.

(3) Mazin, I.; The PRX Editors. Editorial: Altermagnetism−A New Punch Line of Fundamental Magnetism. *Phys. Rev. X* **2022**, *12*, No. 040002.

(4) Mazin, I. Altermagnetism Then and Now. *Physics* **2024**, *17*, No. 4.

(5) Krempaský, J.; Šmejkal, L.; D'Souza, S. W.; Hajlaoui, M.; Springholz, G.; Uhlířová, K.; Alarab, F.; Constantinou, P. C.; Strocov, V.; Usanov, D.; et al. Altermagnetic lifting of Kramers spin degeneracy. *Nature* **2024**, *626*, 517−522.

(6) Zhu, Y.-P.; Chen, X.; Liu, X.; Liu, Y.; Liu, P.; Zha, H.; Qu, G.; Hong, C.; Li, J.; Jiang, Z.; et al. Observation of plaid-like spin splitting in a noncoplanar antiferromagnet. *Nature* **2024**, *626*, 523−528.

(7) Šmejkal, L.; González-Hernández, R.; Jungwirth, T.; Sinova, J. Crystal time-reversal symmetry breaking and spontaneous Hall effect in collinear antiferromagnets. *Sci. Adv.* **2020**, *6*, No. eaaz8809.

(8) Naka, M.; Hayami, S.; Kusunose, H.; Yanagi, Y.; Motome, Y.; Seo, H. Spin current generation in organic antiferromagnets. *Nat. Commun.* **2019**, *10*, No. 4305.

(9) Ma, H.-Y.; Hu, M.; Li, N.; Liu, J.; Yao, W.; Jia, J.; Liu, J. Multifunctional antiferromagnetic materials with giant piezomagnetism and noncollinear spin current. *Nat. Commun.* **2021**, *12*, No. 2846.

(10) Chen, X.; Wang, D.; Li, L.; Sanyal, B. Giant spin-splitting and tunable spin-momentum locked transport in room temperature collinear antiferromagnetic semimetallic CrO monolayer. *Appl. Phys. Lett.* **2023**, *123*, No. 022402.

(11) Gao, Z.; Qu, S.; Zeng, B.; Liu, Y.; Wen, J.; Sun, H.; Guo, P.; Lu, Z. AI-Accelerated Discovery of Altermagnetic Materials. 2023, arXiv:2311.04418. arXiv.org e-Printarchive. https://arxiv.org/abs/2311.04418.

(12) Sødequist, J.; Olsen, T. Two-dimensional altermagnets from high throughput computational screening: Symmetry requirements, chiral magnons, and spin-orbit effects. *Appl. Phys. Lett.* **2024**, *124*, No. 182409.

(13) Zhou, H.-C.; Long, J. R.; Yaghi, O. M. Introduction to Metal−Organic Frameworks. *Chem. Rev.* **2012**, *112*, 673−674.

(14) Song, X.; Liu, J.; Zhang, T.; Chen, L. 2D conductive metal-organic frameworks for electronics and spintronics. *Sci. China Chem.* **2020**, *63*, 1391−1401.

(15) Wang, H.; Zhang, C.; Dong, B.; Zhong, D.; Lu, T. Metal-organic layers: Preparation and applications. *Sci. China Mater.* **2023**, *66*, 839−858.

(16) Thorarinsdottir, A. E.; Harris, T. D. Metal−Organic Framework Magnets. *Chem. Rev.* **2020**, *120*, 8716−8789.

(17) Chakraborty, G.; Park, I. H.; Medishetty, R.; Vittal, J. J. Two-Dimensional Metal-Organic Framework Materials: Synthesis, Structures, Properties and Applications. *Chem. Rev.* **2021**, *121*, 3751−3891.

(18) Gu, X.; Guo, L.; Qin, Y.; Yang, T.; Meng, K.; Hu, S.; Sun, X. Challenges and Prospects of Molecular Spintronics. *Precis. Chem.* **2024**, *2*, 1−13.

(19) Li, W.; Sun, L.; Qi, J.; Jarillo-Herrero, P.; Dincă, M.; Li, J. High temperature ferromagnetism in π-conjugated two-dimensional metal−organic frameworks. *Chem. Sci.* **2017**, *8*, 2859−2867.

(20) Lobo-Checa, J.; Hernández-López, L.; Otrokov, M. M.; Piquero-Zulaica, I.; Candia, A. E.; Gargiani, P.; Serrate, D.; Delgado, F.; Valvidares, M.; Cerdá, J.; et al. Ferromagnetism on an atom-thick & extended 2D metal-organic coordination network. *Nat. Commun.* **2024**, *15*, No. 1858.

(21) Perlepe, P.; Oyarzabal, I.; Voigt, L.; Kubus, M.; Woodruff, D. N.; Reyes-Lillo, S. E.; Aubrey, M. L.; Négrier, P.; Rouzières, M.; Wilhelm, F.; et al. From an antiferromagnetic insulator to a strongly correlated metal in square-lattice $MCl_2(pyrazine)_2$ coordination solids. *Nat. Commun.* **2022**, *13*, No. 5766.

(22) Li, X.; Yang, J. Realizing Two-Dimensional Magnetic Semiconductors with Enhanced Curie Temperature by Antiaromatic Ring Based Organometallic Frameworks. *J. Am. Chem. Soc.* **2019**, *141*, 109−112.

(23) Perlepe, P.; Oyarzabal, I.; Mailman, A.; Yquel, M.; Platunov, M.; Dovgaliuk, I.; Rouzières, M.; Négrier, P.; Mondieig, D.; Suturina, E. A.; et al. Metal-organic magnets with large coercivity and ordering temperatures up to 242 °C. *Science* **2020**, *370*, 587−592.

(24) Lv, H.; Li, X.; Wu, D.; Liu, Y.; Li, X.; Wu, X.; Yang, J. Enhanced Curie Temperature of Two-Dimensional Cr(II) Aromatic Heterocyclic Metal−Organic Framework Magnets via Strengthened Orbital Hybridization. *Nano Lett.* **2022**, *22*, 1573−1579.

(25) Li, X.; Liu, Q.; Tang, Y.; Li, W.; Ding, N.; Liu, Z.; Fu, H.; Dong, S.; Li, X.; Yang, J. Quintuple Function Integration in Two-Dimensional Cr(II) Five-Membered Heterocyclic Metal Organic

Frameworks via Tuning Ligand Spin and Lattice Symmetry. *J. Am. Chem. Soc.* **2023**, *145*, 7869−7878.
(26) Che, Y.; Lv, H.; Wu, X.; Yang, J. Realizing altermagnetism in two-dimensional metal-organic framework semiconductors with electric-field-controlled anisotropic spin current. *Chem. Sci.* **2024**, *15*, 13853−13863.
(27) Li, J.; Li, X.; Yang, J. Chemically Controlled Reversible Magnetic Phase Transition in Two-Dimensional Organometallic Lattices. *Nano Lett.* **2023**, *23*, 9126−9132.
(28) Misumi, Y.; Yamaguchi, A.; Zhang, Z.; Matsushita, T.; Wada, N.; Tsuchiizu, M.; Awaga, K. Quantum Spin Liquid State in a Two-Dimensional Semiconductive Metal-Organic Framework. *J. Am. Chem. Soc.* **2020**, *142*, 16513−16517.
(29) Wang, Z.; Gibertini, M.; Dumcenco, D.; Taniguchi, T.; Watanabe, K.; Giannini, E.; Morpurgo, A. F. Determining the phase diagram of atomically thin layered antiferromagnet $CrCl_3$. *Nat. Nanotechnol.* **2019**, *14*, 1116−1122.
(30) Li, J.; Wu, R. Metal−organic frameworks: possible new two-dimensional magnetic and topological materials. *Nanoscale* **2020**, *12*, 23620−23625.
(31) Yang, C.; Dong, R.; Wang, M.; Petkov, P. S.; Zhang, Z.; Wang, M.; Han, P.; Ballabio, M.; Bräuninger, S. A.; Liao, Z.; et al. A semiconducting layered metal-organic framework magnet. *Nat. Commun.* **2019**, *10*, No. 3260.
(32) Yates, K. *Hückel Molecular Orbital Theory*; Elsevier, 2012.
(33) Ramsden, C. A. Non-bonding molecular orbitals and the chemistry of non-classical organic molecules. *Chem. Soc. Rev.* **1994**, *23*, 111−118.
(34) Živković, T. Calculation of the Non-Bonding Molecular Orbitals in the Hilckel Theory. *Croat. Chem. Acta* **1972**, *44*, 351−364.
(35) Luo, Y.; Bag, S.; Zaremba, O.; Cierpka, A.; Andreo, J.; Wuttke, S.; Friederich, P.; Tsotsalas, M. MOF Synthesis Prediction Enabled by Automatic Data Mining and Machine Learning. *Angew. Chem., Int. Ed.* **2022**, *61*, No. e202200242.
(36) Baranowski, D.; Thaler, M.; Brandstetter, D.; Windischbacher, A.; Cojocariu, I.; Mearini, S.; Chesnyak, V.; Schio, L.; Floreano, L.; Gutiérrez Bolaños, C.; et al. Emergence of Band Structure in a Two-Dimensional Metal−Organic Framework upon Hierarchical Self-Assembly. *ACS Nano* **2024**, *18*, 19618−19627.
(37) Mearini, S.; Baranowski, D.; Brandstetter, D.; Windischbacher, A.; Cojocariu, I.; Gargiani, P.; Valvidares, M.; Schio, L.; Floreano, L.; Puschnig, P.; et al. Band Structure Engineering in 2D Metal−Organic Frameworks. *Adv. Sci.* **2024**, *11*, No. 2404667.
(38) Mounet, N.; Gibertini, M.; Schwaller, P.; Campi, D.; Merkys, A.; Marrazzo, A.; Sohier, T.; Castelli, I. E.; Cepellotti, A.; Pizzi, G.; Marzari, N. Two-dimensional materials from high-throughput computational exfoliation of experimentally known compounds. *Nat. Nanotechnol.* **2018**, *13*, 246−252.
(39) Wang, V.; Tang, G.; Liu, Y.; Wang, R.; Mizuseki, H.; Kawazoe, Y.; Nara, J.; Geng, W. T. High-Throughput Computational Screening of Two-Dimensional Semiconductors. *J. Phys. Chem. Lett.* **2022**, *13*, 11581−11594.
(40) Litvin, D. B. Spin point groups. *Acta Crystallogr., Sect. A* **1977**, *33*, 279−287.
(41) Yuan, L.-D.; Wang, Z.; Luo, J.; Zunger, A. Prediction of low-Z collinear and noncollinear antiferromagnetic compounds having momentum-dependent spin splitting even without spin-orbit coupling. *Phys. Rev. Mater.* **2021**, *5*, No. 014409.
(42) Okugawa, T.; Ohno, K.; Noda, Y.; Nakamura, S. Weakly spin-dependent band structures of antiferromagnetic perovskite $LaMO_3$ (M = Cr, Mn, Fe). *J. Phys.: Condes. Matter* **2018**, *30*, No. 075502.
(43) Kim, H. H.; Yang, B.; Li, S.; Jiang, S.; Jin, C.; Tao, Z.; Nichols, G.; Sfigakis, F.; Zhong, S.; Li, C.; et al. Evolution of interlayer and intralayer magnetism in three atomically thin chromium trihalides. *Proc. Natl. Acad. Sci. U.S.A.* **2019**, *116*, 11131−11136.
(44) Bertolazzi, S.; Brivio, J.; Kis, A. Stretching and Breaking of Ultrathin MoS_2. *ACS Nano* **2011**, *5*, 9703−9709.

https://doi.org/10.1021/jacsau.4c01150
JACS Au 2025, 5, 381−387